

Rapid ortho-to-para nuclear spin conversion of H₂ on a silicate dust surface

M. Tsuge¹, T. Namiyoshi¹, K. Furuya², T. Yamazaki¹, A. Kouchi¹, N. Watanabe^{1*}

¹Institute of Low Temperature Science, Hokkaido University, Sapporo, Hokkaido 060-0819, Japan

²National Astronomical Observatory of Japan, Osawa 2-21-1, Mitaka, Tokyo 181-8588, Japan

*e-mail: watanabe@lowtem.hokudai.ac.jp

Abstract

The H₂ molecule has two nuclear spin isomers, the so-called ortho and para isomers. Nuclear spin conversion (NSC) between these states is forbidden in the gas phase. The energy difference between the lowest ortho and para states is as large as 14.7 meV, corresponding to ~170 K. Therefore, each state of H₂ differently affects not only the chemistry but also the macroscopic gas dynamics in space, and thus, the ortho-to-para abundance ratio (OPR) of H₂ has significant impacts on various astronomical phenomena. For a long time, the OPR of nascent H₂ upon formation on dust grains has been assumed to have a statistical value of three and to gradually equilibrate in the gas phase at the temperature of the circumstances. Recently, NSC of H₂ was experimentally revealed to occur on water ice at very low temperatures and thus incorporated into gas-dust chemical models. However, H₂ molecules should form well before dust grains are coated by water ice. Information about how the OPR of H₂ behaves on bare silicate dust before ice-mantle formation is lacking. Knowing the influence of the OPR of H₂ if the OPR changes even

on a bare silicate surface within an astronomically meaningful time scale is desirable. We report the first laboratory measurements of NSC of H₂ physisorbed on amorphous silicate (Mg₂SiO₄) at temperatures up to 18 K. The conversion was found to occur very rapidly.

Unified Astronomy Thesaurus concepts: Astrochemistry (75); Molecular clouds (1072); Dense interstellar clouds (371); Interstellar molecules (849); Interstellar dust (836); Laboratory astrophysics (2004);

1. Introduction

The H_2 molecule consists of two protons and thus has a total nuclear spin of 0 or 1 with multiplicities of singlet and triplet, respectively. According to the Pauli exclusion principle, the nuclear spin states of 1 (ortho) and 0 (para) are only coupled with the rotational states of odd and even quantum numbers, respectively. In thermal equilibrium, the ortho-to-para abundance ratio (OPR) is expressed by the ratio of rotational Boltzmann distributions for odd and even rotational numbers with spin degeneracies. At temperatures above approximately 200 K, the OPR almost reaches a statistical value of three, while at the low-temperature limit, it becomes zero. The energetically lowest ortho state with rotational number $J = 1$ lies approximately 14.7 meV above the para state with $J = 0$. In the gas phase, radiative transition between these two states is forbidden and, thus, nuclear spin conversion (NSC) only occurs via spin exchange reactions with protons or hydrogen atoms. The conversion timescale due to these processes in molecular clouds (MCs) is as slow as approximately 10^5 – 10^7 yr (Wilgenbus et al. 2000; Flower, Pineau Des Forêts, & Walmsley 2006). Therefore, H_2 molecules in each state can be considered energetically different species. Because of the large energy gap between the ortho and para states, the OPR of H_2 has important astronomical meaning. For example, the OPR affects the gas dynamics of core formation in star-forming regions because the heat capacity of H_2 gas is different between the ortho and para states (Vaytet, Tomida, & Chabrier 2014). Because of the slow conversion between two spin isomers, the OPR of H_2 has been used as a tracer of the age of clouds (Pagani et al. 2013). In cold (~ 10 K) regions such as an MC, the OPR can control the chemical evolution. One of the most discussed issues is the effect of the OPR on the deuterium fractionation of molecules in the gas phase (Bovino et al. 2017). The ionic species H_3^+ is involved in the formation of various interstellar molecules. Once

H_3^+ is deuterated by an ion-molecule reaction, $\text{H}_3^+ + \text{HD} \rightarrow \text{H}_2\text{D}^+ + \text{H}_2$, it works as a dominant deuterium fractionation pathway in MCs. When reactant H_3^+ and products H_2D^+ and H_2 are all in the para state, this reaction is exothermic by 230 K. However, if H_2 is in the ortho state, then the exothermicity is significantly reduced, resulting in the occurrence of a reverse process that destroys H_2D^+ even in MCs.

In contrast to processes in the gas phase, little is known about how the OPR of H_2 behaves on dust grains. H_2 has been widely accepted to predominantly form via H-H recombination on the surface of dust grains (Wakelam et al. 2017). Furthermore, H_2 molecules in the gas phase inevitably collide and interact with dust grains. Nevertheless, processes on dust surfaces concerning the OPR of H_2 remained unclear for a long time because of the difficulties in both experimental and theoretical approaches. Recently, several experiments finally shed light on the behavior of the H_2 OPR on ice surfaces (Sugimoto & Fukutani 2011; Ueta et al. 2016). The OPR of nascent H_2 formed by H-H recombination was revealed to be almost 3, and NSC can occur on water ice within approximately 10^3 s depending on the temperature (Ueta et al. 2016; Watanabe et al. 2010). These experimental findings have now been incorporated into gas-dust chemical models (Bovino et al. 2017; Furuya et al. 2019). However, H_2 formation should be activated and equilibrate on base silicate or carbonaceous dust well before ice-mantle formation. Therefore, knowing whether NSC occurs to change the OPR of H_2 on these surfaces is highly desirable.

2. Experiment

The experiments were performed in an ultrahigh vacuum chamber ($\sim 10^{-8}$ Pa) with a doubly differentially pumped molecular beam source. An amorphous silicate film was deposited on an aluminum substrate by pulsed laser ablation of an Mg_2SiO_4 target in situ; the preparation and characterization of the film are described in Appendix (section A.1). The substrate was located at the center of the main chamber and could be cooled by a closed-cycle helium refrigerator.

The NSC of H_2 on the Mg_2SiO_4 surface was investigated with a combination of temperature programmed desorption (TPD) and resonance-enhanced multiphoton ionization (REMPI) techniques: the TPD-REMPI method. The timing chart for TPD-REMPI experiments is shown in Figure 1. The temperature of the substrate was measured with a silicon diode and controlled with a fluctuation of less than 0.5 K. Prior to each measurement, the substrate was warmed to 55 K to remove O_2 molecules from the surface since O_2 molecules are known to enhance the ortho-to-para conversion of H_2 . At temperatures of 10–18 K, H_2 molecules with an OPR of 3 were deposited on the substrate as a pulsed molecular beam (~ 300 μs pulse duration, 200 Hz, 3000 shots) with an incident angle of 45° with respect to the surface normal. The pulsed H_2 beam was produced by expansion of normal H_2 gas (300 kPa) through a pulsed valve (100 μm -diameter orifice), skimmed by a skimmer, and introduced into the main chamber through an orifice of 1–2 mm. By using an H_2 molecular beam instead of a continuous beam, the deposition duration is significantly reduced so that the ortho-to-para conversion during deposition is suppressed. An increase in undesired background H_2 in the chamber is also avoided. Therefore, the use of pulsed molecular beam suppresses NSC due to gas-phase secondary processes and NSC on the coldhead (i.e., metal surfaces). At 10 K, the H_2 dose was

approximately 3×10^{14} molecules cm^{-2} , corresponding to an H_2 coverage of approximately 0.03, at which the interaction between H_2 molecules would be negligible. After a certain waiting time, $t_{\text{w.t.}}$, of 10–810 s, the sample was warmed to 55 K at a ramp rate of 20 K min^{-1} : the TPD method. The desorbing H_2 molecules were ionized by the REMPI method and detected with a time-of-flight spectrometer. Laser radiation in a wavelength range of 201–203 nm was provided by an Nd^{3+} :YAG laser-pumped dye laser with subsequent frequency doubling and mixing in potassium dihydrogen phosphate and beta barium borate crystals, respectively. In this wavelength range, H_2 molecules can be rotational-state-selectively ionized by $(2 + 1)$ REMPI via the $E, F^1(v' = 0, J' = J'') \leftarrow X^1(v'' = 0, J'' = 0 \text{ or } 1)$ transition. The REMPI laser was focused by a plano-convex lens with $f = 300 \text{ mm}$ approximately 1.0 mm above the sample surface. In this paper, we call the H_2 signal detected during a TPD run a TPD-REMPI signal. At low temperatures, *ortho*- H_2 (*o*- H_2) and *para*- H_2 (*p*- H_2) are in the $J = 1$ and $J = 0$ states, respectively, and thus, we measured TPD-REMPI signals for these states.

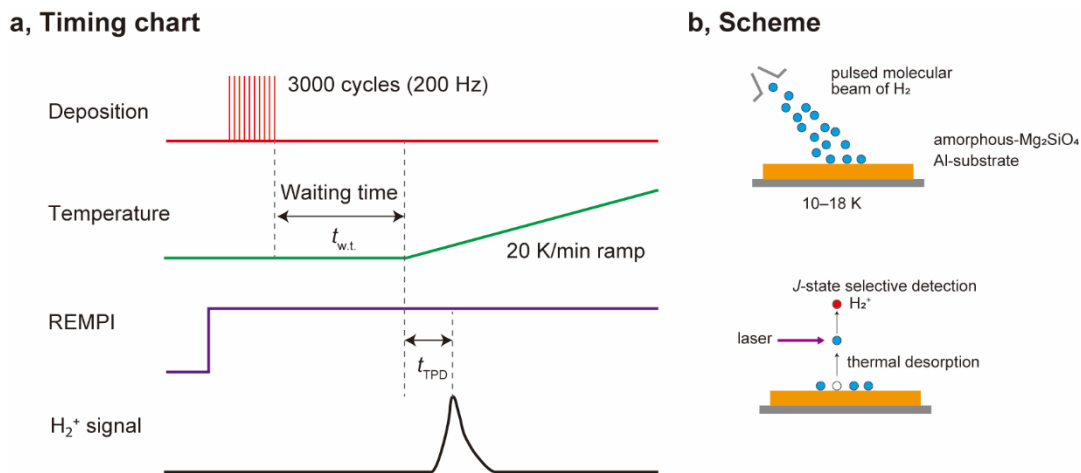


Figure 1. Schematic of the TPD-REMPI experiment. a, Timing chart of the TPD-REMPI experiment. A series of molecular beam pulses of normal H₂ are first deposited on an Mg₂SiO₄ sample maintained at 10–18 K. After a certain waiting time ($t_{w.t.}$, 10–810 s), the temperature of the substrate is raised at a 20 K min⁻¹ ramping rate; this process is the so-called temperature-programmed desorption (TPD) process. The laser for REMPI is always operating during each run with a 10 Hz repetition rate and a pulse energy of 200 μJ pulse⁻¹. The H₂ molecules desorbed during a TPD run, i.e., at $t = t_{w.t.} + t_{TPD}$, are rotational-state-selectively ionized to H₂⁺ by the REMPI laser and detected with a linear time-of-flight spectrometer. b, Schematic for the H₂ deposition (top) and TPD-REMPI (bottom) processes.

3. Results and Discussion

3.1 Determination of NSC Time Constants

The experimental results obtained at 10 K are presented in Figure 2. Figure 2a shows a series of TPD-REMPI data measured for $t_{\text{w.t.}} = 10, 410, \text{ and } 810$ s. The growth of the $J=0$ signal and decay of the $J=1$ signal with increasing $t_{\text{w.t.}}$ are readily recognized. The time variation of integrated TPD-REMPI signals is plotted in Figure 2b. The sum of the $J=0$ and $J=1$ signals is constant within the experimental error, ensuring that accumulation of background H_2 during the waiting time and desorption upon NSC are negligible. Consequently, the decay of the $J=1$ signal is attributed to the ortho-to-para conversion.

When the temperature of the substrate is sufficiently low such that thermal desorption can be ignored, the number density of $o\text{-H}_2$ ($J=1$) decreases with time due to ortho-to-para conversion, while that of $p\text{-H}_2$ ($J=0$) increases. This situation is applicable to temperatures of 10, 12, and 14 K in the present experiments. Thus, if one monitors the number density, $[o\text{-H}_2]_t$, it shows a single exponential decay

$$[o\text{-H}_2]_t = [o\text{-H}_2]_0 \exp(-k_{\text{OP}}t), \quad (1)$$

where k_{OP} is the ortho-to-para conversion rate constant and $[o\text{-H}_2]_t + [p\text{-H}_2]_t = [o\text{-H}_2]_0 + [p\text{-H}_2]_0 = \text{const.}$ Fitting of the decay of the $J=1$ TPD-REMPI signal by a single exponential function gives a decay time constant ($1/k_{\text{OP}}$) of 980 ± 90 s at 10 K. The OPR, ~ 1.8 , for $t_{\text{w.t.}} = 10$ s is already smaller than the statistical value of 3 because NSC proceeds even during the TPD run. As detailed in section A.2, this enhancement has little effect on the obtained time constants.

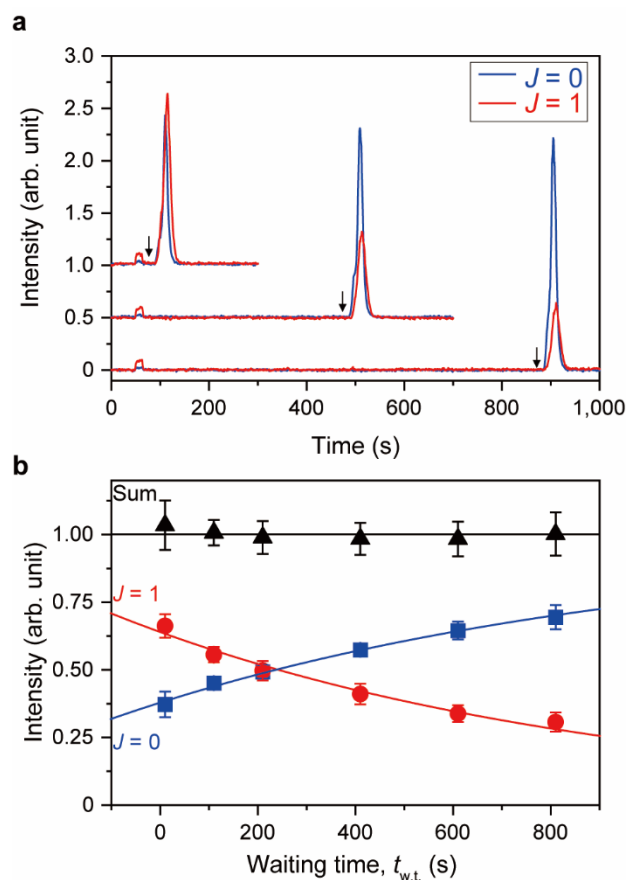


Figure 2. Time evolution of *o*- and *p*-H₂ populations at 10 K. a, H₂ intensities for $J = 0$ (blue) and $J = 1$ (red) detected by the REMPI method at different waiting times (from top to bottom, 10, 410, and 810 s). The weak signals at 50–65 s are due to gaseous H₂ supplied from the molecular beam source. The starting time of each TPD run is indicated by vertical arrows. b, Time evolution of TPD-REMPI signals for $J = 0$ (blue square), $J = 1$ (red circle), and their sum (black triangle). The intensities were obtained by integrating the TPD-REMPI signal. The error bars represent the statistical errors among 5 respective measurements. Solid curves are the results of single exponential fitting.

The time variation of TPD-REMPI signals for temperatures of 12, 14, 16, and 18 K are presented in Figure 3. As shown in Figures 3a and 3b, the sum of the $J = 0$ and $J = 1$ TPD-REMPI signals is constant at 12 and 14 K, similar to the case at 10 K. Thus, the decay of $J = 1$ TPD-REMPI signal can be fitted by Equation (1) to obtain decay time constants of 560 ± 60 and 360 ± 20 s for 12 and 14 K, respectively.

At 16 and 18 K (Figures 3c and 3d), decay of the sum as a function of $t_{w.t.}$ is observed. This decay is presumably due to thermal desorption during the waiting time. In this case, differential rate equations for the surface number densities of $o\text{-H}_2$ and $p\text{-H}_2$ are written as follows:

$$\frac{d[o\text{-H}_2]}{dt} = -k_{\text{sub}}[o\text{-H}_2] - k_{\text{OP}}[o\text{-H}_2], \quad (2)$$

$$\frac{d[p\text{-H}_2]}{dt} = -k_{\text{sub}}[p\text{-H}_2] + k_{\text{OP}}[o\text{-H}_2], \quad (3)$$

where k_{sub} is the rate constant for unimolecular sublimation, which is assumed to be the same for $o\text{-H}_2$ and $p\text{-H}_2$; in reality, k_{sub} for $o\text{-H}_2$ might be smaller because of a slightly large binding energy, as deduced from the TPD spectra. Equation (2) is readily integrated to become

$$[o\text{-H}_2] = [o\text{-H}_2]_0 e^{-(k_{\text{sub}} + k_{\text{OP}})t}. \quad (4)$$

An integration of the sum of Equations (2) and (3) gives the following equation for the total H_2 on the surface:

$$[\text{H}_2]_t = [o\text{-H}_2]_t + [p\text{-H}_2]_t = [\text{H}_2]_0 e^{-k_{\text{sub}}t}. \quad (5)$$

Therefore, the sublimation rate constant (k_{sub}) is obtained from single exponential fitting of the decay of $[\text{H}_2]_t$ (i.e., the sum of $[o\text{-H}_2]_t$ and $[p\text{-H}_2]_t$), and $k_{\text{sub}} + k_{\text{OP}}$ is obtained from fitting of the decay of $[o\text{-H}_2]_t$. Consequently, the ortho-to-para conversion time constant, $1/k_{\text{OP}}$, is determined. Accordingly, the time constant for NSC was extracted from the

fitting of $J = 1$ and the sum to be 290 ± 20 and 260 ± 70 s for 16 and 18 K, respectively, whereas the time constants for sublimation ($1/k_{\text{sub}}$) were 3300 ± 200 and 400 ± 80 s.

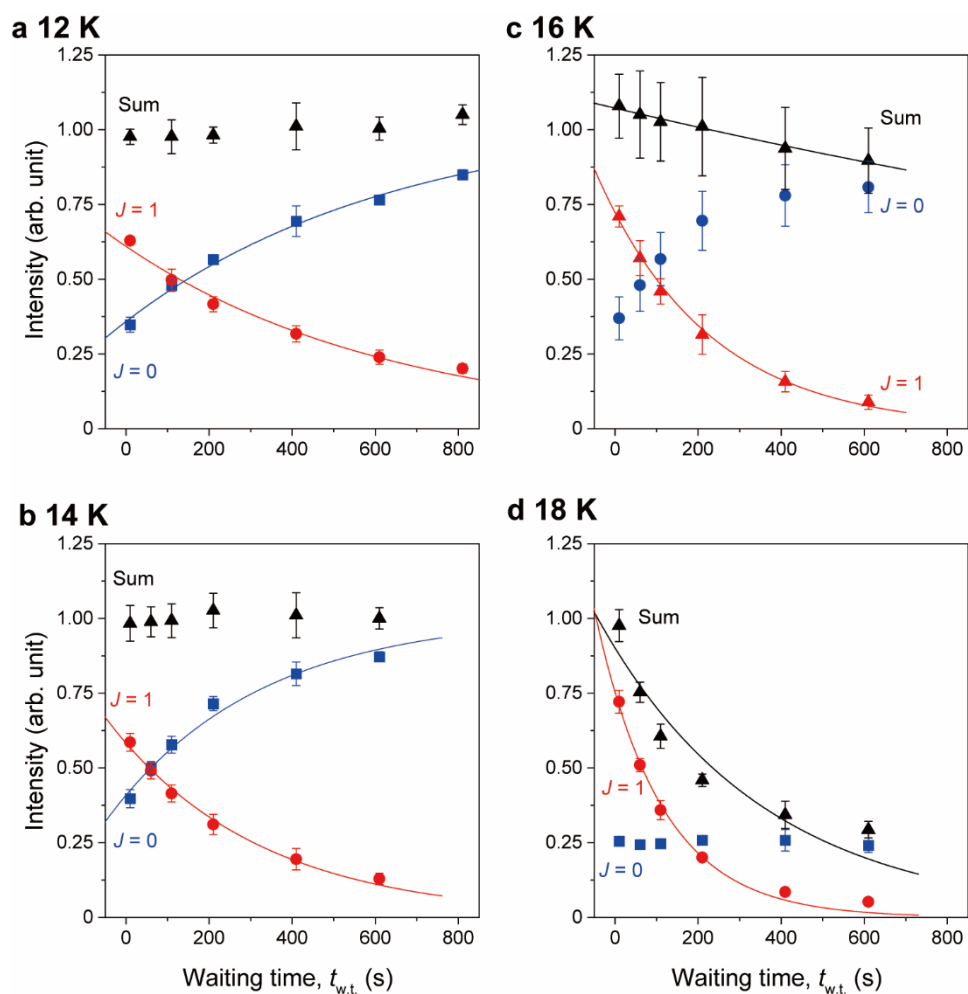


Figure 3. Time evolution of TPD-REMPI intensities for $J=0$, $J=1$, and their sum. a, b, c, and d, Time evolution of TPD-REMPI signals for $J=0$ (blue square), $J=1$ (red circle), and their sum (black triangle) at temperatures of 12, 14, 16, and 18 K, respectively. The intensities were obtained by integrating the TPD-REMPI signal. The error bars represent the statistical errors among 5 respective measurements. Solid curves are the results of single exponential fitting.

3.2 Comparison of NSC Time Constants

The NSC time constants determined in this work for an amorphous Mg_2SiO_4 surface are plotted as a function of substrate temperature in Figure 4, together with those reported for an amorphous solid water (ASW) surface (Ueta et al. 2016). These time constants are listed in Table 1. The time constants for the Mg_2SiO_4 surface are smaller than those for the ASW surface by a factor of 2–3. In the case of ASW, the time constant significantly decreases in the 9.2 to 12 K region and remains constant above 12 K. In the case of Mg_2SiO_4 , we observe a gradual decrease in time constant as a function of temperature in the investigated temperature range (10–18 K). Because of fast unimolecular sublimation, we were unable to determine the time constant above 18 K. However, an analysis described in section A.2 indicates that the time constant would not be smaller than 200 s even at the sublimation temperature (20–26 K) in the TPD runs. For comparison, we measured the NSC of D_2 at 18 K (section A.3). The time constant is much larger than that of H_2 at 18 K, consistent with previous experiments on ASW (Sugimoto & Fukutani 2011; Ueta et al. 2016).

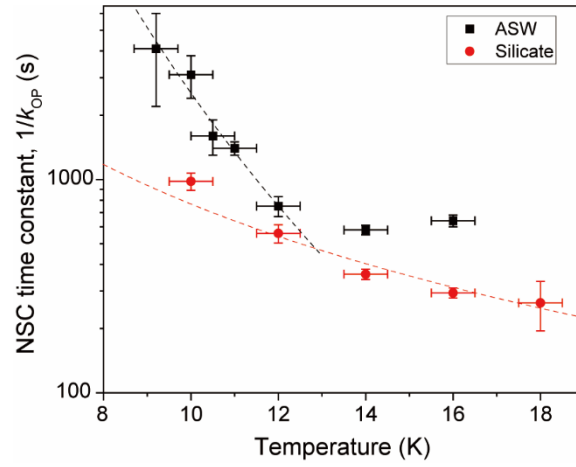


Figure 4. Ortho-to-para conversion time constants on silicate (amorphous Mg_2SiO_4) and ASW. The temperature dependences of the ortho-to-para conversion time constants ($1/k_{OP}$) for silicate (this work) and ASW (Ueta et al. 2016) are plotted. Vertical error bars represent the errors originating from the decay curve fitting. Horizontal error bars represent the temperature fluctuation in the experiments. Dashed lines represent the results of fitting assuming the $k_{OP} \propto T^n$ relation (Scott & Jeffries 1962). For amorphous silicate, $n = 1.9 \pm 0.3$ was obtained for the temperature range 10–18 K, while, for ASW, $n = 7.1 \pm 0.6$ for the range 9.2–12 K. Time constants are summarized in Table 1.

Table 1. NSC time constants determined for H₂ on amorphous Mg₂SiO₄ and ASW surfaces at various temperatures.

Temperature (K)	NSC time constant (s)	
	Mg ₂ SiO ₄	ASW ^a
9.2		4,100 ± 1,900
10	980 ± 90	3,100 ± 700
10.5		1,600 ± 300
11		1,400 ± 100
12	560 ± 60	750 ± 80
14	360 ± 20	580 ± 30
16	290 ± 20	640 ± 40
18	260 ± 70	

^aUeta et al. 2016.

3.3 Temperature-dependence of NSC Rate

The ortho-to-para conversion of H₂ on surface involves the NSC and subsequent energy dissipation processes. The presence of magnetic field is known to enhance the NSC process (Fukutani & Sugimoto 2011). Because an Mg₂SiO₄ film does not have magnetic moment and an adsorption of paramagnetic O₂ molecules is avoided, such an enhancement would be negligible in the present experiment. However, we cannot exclude magnetic moment induced by defects near the sample surface. To discuss the effect of such magnetic moments, an extensive surface characterization is required. The mechanisms of NSC on nonmagnetic surface have been theoretically discussed in recent years but those are not yet conclusive (Fukutai & Sugimoto 2011; Ilisca 2018; Ilisca & Ghiglieno 2014). Clarifying it is out of the scope of this paper. Here, we focus our discussion on the mechanism of energy dissipation process required for the NSC. The energy gap between the $J = 1$ and $J = 0$ states is 14.7 meV (≈ 170 K) for the isolated H₂ but may become smaller due to the suppression of rotational motion for H₂ adsorbates. Therefore, the corresponding energy should be released into the solid. The presence of temperature dependence (Figure 4) indicates that phonons play a role in the energy dissipation process.

Spin-lattice relaxation will occur through one-phonon or two-phonon processes. In the one-phonon process, the excess energy associated with the NSC process is transferred to the surroundings (i.e., phonon excitation in the thermal bath). Depending on the energy matching condition between the excess energy and phonon modes of the surroundings, the one-phonon process shows two distinct temperature dependences (Scott & Jeffries 1962). When there is a satisfactory match between them, the one-phonon process is known to show a temperature dependence of NSC rate as $k_{OP}(T) =$

$A \times \coth\left(\frac{\delta}{2T}\right)$, where T is the solid temperature and δ is the energy gap between these two spin states. On the other hand, when there is a mismatch between them, the process becomes a slower phonon-limited “bottle-neck” process. This process shows a distinct temperature dependence, $k_{\text{OP}}(T) = A \times T^n$ ($n \sim 2$).

The two-phonon process proceeds via the simultaneous absorption (from the initial state ($J = 1$) to the intermediate state) and emission (from the intermediate state to the final state ($J = 0$)) of phonons. Based on whether the intermediate state is real (i.e., $J = 2$ state) or virtual, the process is classified into Orbach process or Raman process, respectively. The NSC rate of Orbach process follows $k_{\text{OP}}(T) = A \times \exp\left(-\frac{\Delta}{T}\right)$, where Δ corresponds to the energy gap between the initial and intermediate states (Scott & Jeffries 1962). On the other hand, the Raman process shows a power law dependence, $k_{\text{OP}}(T) = A \times T^n$ ($n = 7$ or 9). For example, Ueta et al. (2016) attributed the temperature dependence observed for H₂ NSC on ASW to this process (Figure 4).

Among the phonon processes described above, the one phonon process expressed by $k_{\text{OP}}(T) = A \times \coth\left(\frac{\delta}{2T}\right)$ can be excluded because it becomes almost temperature independent in the present experimental condition, where $\delta = 170$ K and 10 K $\leq T \leq 18$ K. The Orbach process ($k_{\text{OP}}(T) = A \times \exp\left(-\frac{\Delta}{T}\right)$) with $\Delta = 399$ K that is the energy gap between $J = 1$ and $J = 2$ (Silvera 1980) was found not to reproduce the observed temperature dependence. Then, we fitted the experimental data by the expression $k_{\text{OP}}(T) = A \times T^n$, which gave $n = 1.9 \pm 0.3$ (see Figure 4). As a result, we attribute the observed temperature dependence to a slower phonon-limited “bottle-neck” process, where one-phonon process dominates over two-phonon Orbach and Raman processes and there is a mismatch between the excess energy associated with the NSC

process and phonon modes of the thermal bath. It is not easy to further discuss the energy matching condition because the exact energy gap for H₂ on Mg₂SiO₄ surface and the surface-phonon frequencies of amorphous Mg₂SiO₄ are not known. Nonetheless, an inelastic neutron scattering study of crystalline Mg₂SiO₄ (Ghose et al. 1987) showed that an Mg₂SiO₄ solid possesses phonon modes in the range 10–40 meV, indicating that the excess energy associated with the direct NSC process (≤ 14.7 meV) can be eventually dissipated into the Mg₂SiO₄ bath. We note that this will not be the sole mechanism that explain a rapid NSC of H₂ on Mg₂SiO₄ surface, since the NSC of molecules on surface is complicated; e.g., several mechanisms have been suggested to explain the observed H₂ NSC rates on ASW (Fukutani & Sugimoto 2011, Ueta et al. 2016, Ilisca 2018).

3.4 Efficiency of ortho-to-para Conversion under Astrophysical Environments

In star-forming regions, almost all hydrogen is present as H₂ in the gas phase rather than on grain surfaces because of the very low H₂-H₂ surface binding energy (~ 100 K (Lee, Gowland, & Reddish 1971)), and because of the limited number of binding sites per H₂ molecule ($\sim 10^{-4}$ site per H₂). Here, we derive the rate ($\text{cm}^{-3} \text{s}^{-1}$) at which NSC on grain surfaces affects the gas-phase H₂ OPR under astrophysical environments using the experimentally derived k_{OP} . We denote the rate as $R_{\alpha \rightarrow \beta}^{\text{surf}}$, where α and β indicate either ortho or para. $R_{\alpha \rightarrow \beta}^{\text{surf}}$ depends on the (i) collision rate of gaseous H₂ with grain surfaces (R_{col}), (ii) sticking probability (S), (iii) ortho-to-para conversion time constant, and (iv) sublimation timescale of adsorbed H₂ and can be described as (Bovino et al. 2017; Fukutani & Sugimoto 2013; Furuya et al. 2019)

$$R_{\alpha \rightarrow \beta}^{\text{surf}} = \eta_{\alpha \rightarrow \beta} (1 - \Theta) S R_{\text{col}}(\alpha\text{-H}_2), \quad (6)$$

where Θ is the fraction of adsorption sites occupied by H_2 . We consider the factor $(1 - \Theta)$ in Equation (6), assuming that only one H_2 molecule is allowed to be adsorbed per adsorption site. Then, the product $(1 - \Theta)SR_{\text{col}}(\alpha\text{-H}_2)$ expresses the adsorption rate of H_2 . The term $\eta_{o \rightarrow p}$ ($\eta_{p \rightarrow o}$) represents the yield of gaseous $o\text{-H}_2$ ($p\text{-H}_2$) per $p\text{-H}_2$ ($o\text{-H}_2$) adsorption, which depends on the competition between NSC and sublimation of adsorbed H_2 . To determine $\eta_{o \rightarrow p}$ under astrophysical environments, we basically follow the procedure developed in our previous work, in which NSC of H_2 on an ASW surface was studied (Furuya et al. 2019).

The surface coverage of H_2 is expected to be in adsorption-desorption equilibrium since the surface adsorption site density is $\sim 10^{16}$ site cm^{-2} and the H_2 fluence (the time integral of the H_2 flux) on grain surfaces reaches this value in a very short timescale (~ 10 ($10^3 \text{ cm}^{-3}/n(\text{H}_2)$) yr) compared to the dynamical timescale (i.e., lifetime of MCs). Under adsorption-desorption equilibrium, the H_2 OPR of the gas desorbing from the surface can be expressed as

$$R_{\text{sub}}(o\text{-H}_2)/R_{\text{sub}}(p\text{-H}_2) = [(1 - \eta_{o \rightarrow p})f_o + \eta_{p \rightarrow o}f_p]/[\eta_{o \rightarrow p}f_o + (1 - \eta_{p \rightarrow o})f_p], \quad (7)$$

where R_{sub} is the sublimation rate of H_2 . f_o and f_p are the fractions of $o\text{-H}_2$ and $p\text{-H}_2$, respectively, in adsorbing H_2 (or equivalently H_2 in the gas phase). With the relation $\eta_{p \rightarrow o} = \eta_{o \rightarrow p}\gamma$, where γ is the thermalized value of the H_2 OPR, one can obtain

$$\eta_{o \rightarrow p} = [f_o - f_p R_{\text{sub}}(o\text{-H}_2)/R_{\text{sub}}(p\text{-H}_2)]/[(f_o - \gamma f_p)(1 + R_{\text{sub}}(o\text{-H}_2)/R_{\text{sub}}(p\text{-H}_2))]. \quad (8)$$

We quantify $R_{\text{sub}}(o\text{-H}_2)$ and $R_{\text{sub}}(p\text{-H}_2)$ using the numerical simulations described below, followed by evaluation of $\eta_{o \rightarrow p}$ and $\eta_{p \rightarrow o}$ from Equation (8).

We numerically solve a set of rate equations for $o\text{-H}_2$ and $p\text{-H}_2$ that describe the adsorption of gaseous H_2 , thermal desorption, thermal hopping, and NSC of adsorbed H_2 , considering various adsorption sites with different potential energy depths on surfaces

(see Equations 6 and 7 in Furuya et al. 2019). Regarding chemical species, only *o*-H₂ and *p*-H₂ in the gas phase and on grain surfaces are considered in this model. Initially, all H₂ is assumed to be in the gas phase with an OPR of 3, i.e., f_o and f_p are 0.75 and 0.25, respectively. For the binding energy distribution of H₂, we use the experimentally determined binding energy distribution of HD on amorphous MgFeSiO₄ in the literature (Figure 5) (He & Vidali 2014). The hopping-to-binding energy ratio (χ) is poorly constrained, and here, we assume a conservative value of 0.8. The choice of the exact value of χ does not significantly affect our simulation results because $\eta_{o \rightarrow p}$ is close to unity even for $\chi = 0.8$ (see below) and because a lower χ tends to lead to a higher $\eta_{o \rightarrow p}$ (Furuya et al. 2019). The sticking probabilities of H₂ to silicate and to ASW are taken from Chaabouni et al. 2012 and He, Acharyya, & Vidali 2016, respectively.

We run a small grid of pseudo-time-dependent simulations (i.e., the gas density and temperature are fixed with time in each simulation), varying the temperature from 10 to 20 K, and evaluate $\eta_{o \rightarrow p}$ using Equation (8). For temperatures from 10 to 18 K, we adopt the measured NSC time constant or the linearly interpolated value. Above 18 K, we assume that the time constant is the same as that at 18 K. As shown in Figure 6a, $\eta_{o \rightarrow p}$ is close to unity, i.e., every *o*-H₂ adsorption leads to NSC, up to 18 K. $\eta_{o \rightarrow p}$ decreases at higher temperatures and is ~ 0.25 at 20 K. For the evaluation of $\eta_{o \rightarrow p}$, we chose the time at which the total H₂ fluence reaches 10^{17} cm^{-2} , corresponding to the duration time of $\sim 100 (10^3 \text{ cm}^{-3}/n(\text{H}_2)) \text{ yr}$. By this time, the H₂ coverage on the surface reaches adsorption-desorption equilibrium under all physical conditions explored here. We confirmed that $\eta_{o \rightarrow p}$ does not change with time once the system reaches adsorption-desorption equilibrium. For an ASW surface, $\eta_{o \rightarrow p}$ is close to unity only at surface temperatures lower than 13 K. The higher $\eta_{o \rightarrow p}$ for silicate than for ASW at a given temperature is

due to (i) the smaller ortho-to-para conversion time constant, as found in this work (Figure 4), and (ii) the higher binding energy (Figure 5).

The yield of p -H₂ per o -H₂ collision with silicate (i.e., $\eta_{o \rightarrow p}(1 - \Theta)S$) is shown in Figure 6b. The yield for silicate takes the maximum value of ~ 0.8 at ~ 14 – 18 K. In other words, every o -H₂ collision with silicate surfaces produces approximately one p -H₂ in the temperature range between 14 K and 18 K; i.e., the timescale in which NSC on grain surfaces affects the gas-phase H₂ OPR ($\tau_{OP} = n(o\text{-H}_2)/R_{o \rightarrow p}^{surf}$) is comparable to the collisional timescale of o -H₂ with grain surfaces ($\sim 3 (10^3 \text{ cm}^{-3}/n_{\text{H}})$ Myr, where n_{H} is the number density of hydrogen nuclei). At warmer temperatures, the residence time of H₂ on surfaces is too short for NSC. At lower temperatures, the exchange of gaseous and icy H₂ is inefficient (i.e., Θ is high; adsorbed H₂ does not desorb and hinders other gaseous H₂ from being adsorbed). At a given temperature, Θ increases with increasing H₂ gas density. This is the reason why the yield is slightly lower at the H₂ gas density of 10^4 cm^{-3} compared to that at 10^3 cm^{-3} .

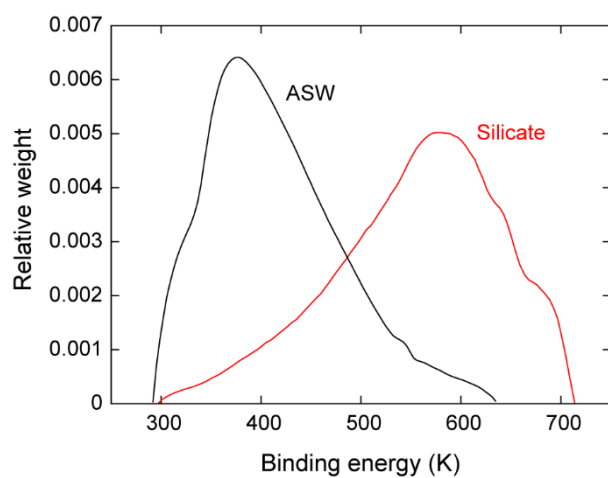


Figure 5. Binding energy distribution of H₂ on surfaces. The binding energy distribution of H₂ on silicate (red line) adopted in our numerical simulations is shown along with that on ASW (black line) for comparison. The data were taken from [He & Vidali 2014](#).

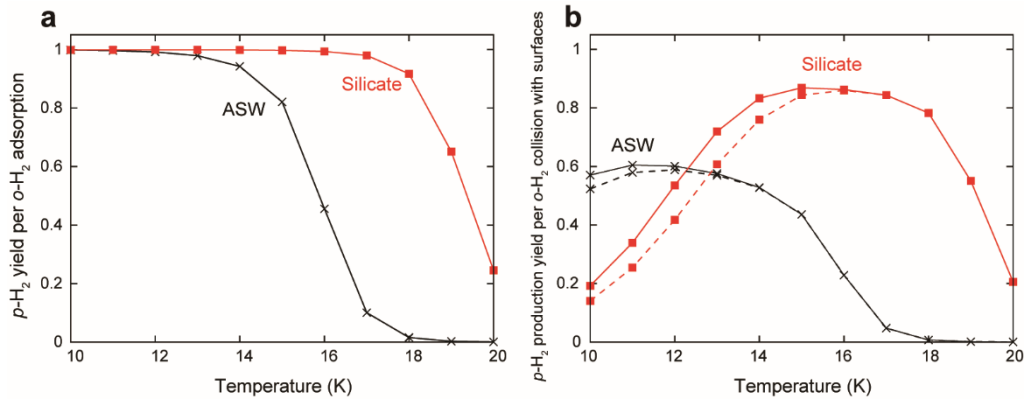


Figure 6. a, Yields of $p\text{-H}_2$ per $o\text{-H}_2$ adsorption ($\eta_{o \rightarrow p}$) as functions of temperature. The red line shows the yield for silicate (this work), while the black line shows that for ASW (Furuya et al. 2019) for comparison. The H_2 gas density is assumed to be 10^3 cm^{-3} , but the density dependence is very weak; the yields at 10^4 cm^{-3} are almost identical to those at 10^3 cm^{-3} . b, Production yields of $p\text{-H}_2$ per $o\text{-H}_2$ collision as functions of temperature. The solid lines represent the values at the H_2 gas density of 10^3 cm^{-3} , while the dashed lines represent the values at 10^4 cm^{-3} .

3.5 Astrophysical Implication

In the ISM, H₂ predominantly forms via recombination of two H atoms on grain surfaces and desorbs into the gas phase. The conversion of H atoms into H₂ molecules finishes before dust grains are coated by ice mantles (e.g., [Hocuk & Cazaux 2015](#); [Furuya et al. 2015](#)). The OPR of H₂ upon formation on the surfaces is three ([Watanabe et al. 2010](#)). The dust temperature observed in the diffuse interstellar medium (ISM) is ~20 K, and it is lower in MCs (15–17 K) ([Planck Collaboration et al. 2014](#)). We expect that NSC of H₂ on bare grain surfaces affects the H₂ OPR from the formation stage of H₂ (i.e., in MCs); the NSC rate ($\tau_{op}^{-1}n(o\text{-H}_2)$) should be comparable or greater than the H₂ formation rate on grains ($R_{\text{form}}(\text{H}_2)$) when $n(o\text{-H}_2) \gtrsim n(\text{atomic H})$ because the H₂ formation rate is given by half the adsorption rate of atomic H on grain surfaces, while the NSC rate is very close to the collisional rate of $o\text{-H}_2$ to the grain surfaces.

To confirm this, we consider a simple model of the evolution of $o\text{-H}_2$ and $p\text{-H}_2$ in the gas phase, where only the H₂ formation on grain surfaces and NSC of H₂ on grain surfaces are taken into account:

$$\frac{dn(o\text{-H}_2)}{dt} = b_o R_{\text{form}}(\text{H}_2) - R_{o \rightarrow p}^{\text{surf}} + R_{p \rightarrow o}^{\text{surf}}, \quad (9)$$

$$\frac{dn(p\text{-H}_2)}{dt} = b_p R_{\text{form}}(\text{H}_2) + R_{o \rightarrow p}^{\text{surf}} - R_{p \rightarrow o}^{\text{surf}}, \quad (10)$$

$$\frac{dn(\text{atomic H})}{dt} = -2R_{\text{form}}(\text{H}_2), \quad (11)$$

where b_o and b_p are the branching ratios to form $o\text{-H}_2$ and $p\text{-H}_2$, respectively, for H₂ formation on grain surfaces. We solve the above ordinary differential equations under the physical conditions appropriate for MCs, $n_{\text{H}} = 10^3 \text{ cm}^{-3}$ and the gas and dust temperatures of 15 K. It should be noted that our model does not consider the formation of ice layers and we assume that dust grains are always bare. In reality, dust grains are covered by ice

at some point, and after that the NSC on bare grains is no more relevant. In the ISM, two types of dust grains exist: silicate and carbonaceous materials. We treat all bare grains as silicate in this model, and the total cross section per H nuclei is set to $1 \times 10^{-21} \text{ cm}^{-2}$. The NSC on amorphous diamond-like carbon surfaces was observed in our previous experiments (Tsuge et al. 2019), but the time constant was not derived. The time evolution of the atomic H and H₂ abundances and the H₂ OPR are shown in Figure 7. As expected, when $n(\text{H}_2) \sim n(\text{atomic H})$, the H₂ OPR is already lower than three. Since the density dependence of $R_{o \rightarrow p}^{surf}$ and $R_{\text{form}}(\text{H}_2)$ is the same, this result does not depend on the chosen density. The results indicate that NSC of H₂ on silicate surfaces is rapid enough to reduce the H₂ OPR to be lower than three when the conversion of H atoms into H₂ occurs in the ISM.

NSC of H₂ also occurs in the gas phase via proton exchange reactions with H⁺ and H₃⁺ (Honvault et al. 2011; Hugo, Asvany, & Schlemmer 2009). After dust grains are covered by ice, NSC of H₂ occurs at least on ASW (Watanabe et al. 2010). In order to reveal the contribution of each process to the evolution of H₂ OPR, astrochemical simulations of the MC formation with the NSC processes of H₂ both on grain surfaces and in the gas phase are demanded. Such studies are postponed for future work.

This work was partly supported by JSPS Grant-in-Aid for Specially promoted Research (JP17H06087), Grant-in-Aid for Scientific Research (C) (JP18K03717), and Grant-in-Aid for Early-Career Scientists (JP17K14245)

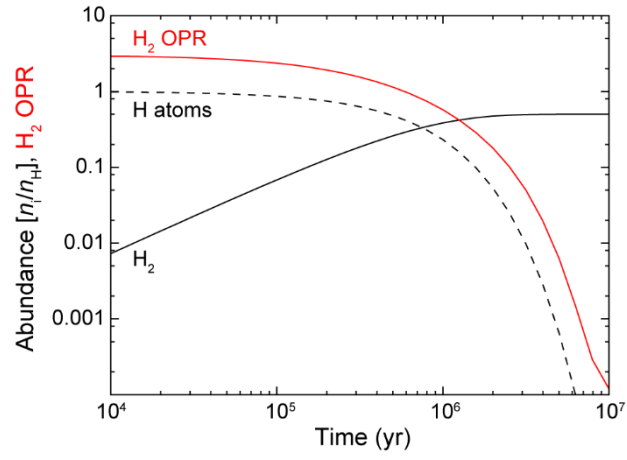


Figure 7. The time evolution of the atomic H (dashed black line) and H₂ (solid black line) abundances and the H₂ OPR (red line) predicted by our simple model (see the main text). The density of hydrogen nuclei (n_{H}) is set to 10^3 cm^{-3} and the gas and dust temperatures are set to 15 K.

Appendix

A.1. Preparation and Characterization of the Amorphous Mg₂SiO₄ Film

The amorphous Mg₂SiO₄ film was prepared on an aluminum substrate by pulsed laser ablation in the main chamber. During sample preparation, an Mg₂SiO₄ target was placed near the aluminum substrate at an approximately 40 mm distance and a 45° angle. The rotating target was irradiated with a pulsed laser beam (532 nm wavelength, 8 ns pulse width, 10 Hz repetition rate, and 20 mJ pulse energy) focused with an $f = 300$ mm lens. Typically, laser ablation was performed for 12,000 pulses, resulting in a few tens of nanometers thick film on the aluminum substrate.

To characterize the samples by transmission electron microscopy (TEM), a thin film of Mg₂SiO₄ was prepared on a thin carbon film with a thickness of less than 6 nm on a copper mesh grid for TEM observation. A TEM apparatus (JEOL, JEM-2100F) was used with a field emission gun at an acceleration voltage of 200 kV, which was equipped with energy dispersive X-ray spectroscopy (EDS) for chemical composition analysis (JEOL, JED2300T). The TEM analysis results are summarized in Figure A1. The bright-field image (Figure A1a) shows that the sample was composed of ~99.7 % homogeneous regions and ~0.3 % high contrast particles by area ratio. The Mg/Si ratio of the homogeneous regions was analyzed by EDS and found to be 1.86. We obtained the electron diffraction patterns of a homogeneous region using a thicker sample fabricated by the same method (Figure A1b). The electron diffraction pattern shows a halo pattern that represents an amorphous structure. The intensity line profile of the electron diffraction pattern (Figure A1b, inset) shows a hump, which probably originates from a peak (2.88 Å) due to amorphous Mg₂SiO₄ (Igami et al. 2020).

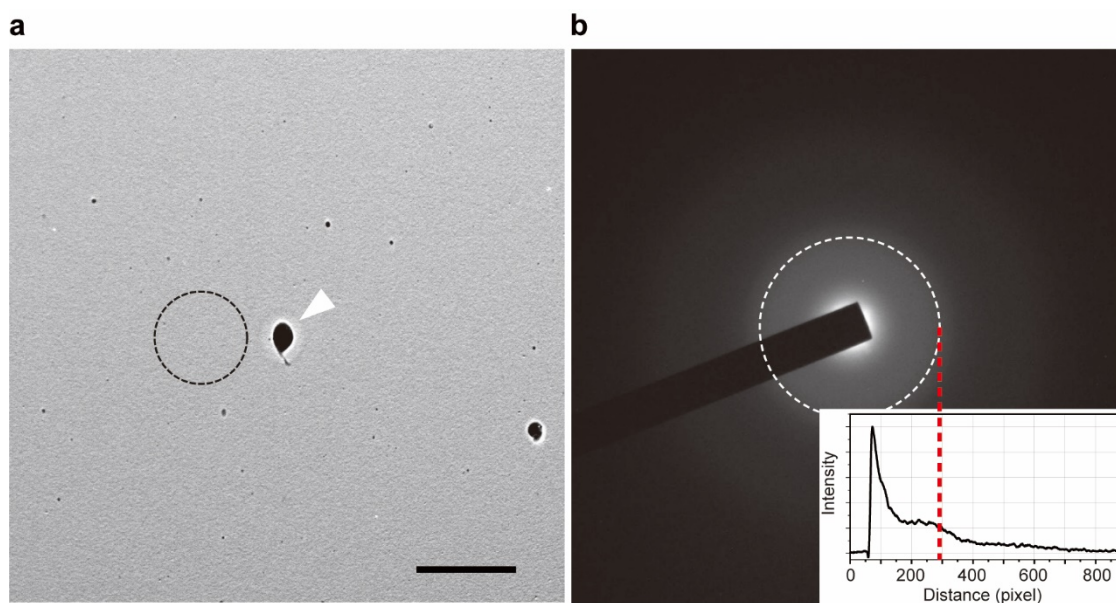


Figure A1. TEM analysis of amorphous Mg_2SiO_4 film. a, Bright-field TEM image of the amorphous Mg_2SiO_4 film. The region enclosed by the black broken line and the particle indicated by white arrowhead were analyzed by EDS, and the Mg/Si ratios are 1.86 and 1.74, respectively. The scale bar is 2 μm . b, Electron diffraction pattern of a homogeneous region in the amorphous Mg_2SiO_4 film. The white broken line corresponds to a d-spacing of 2.88 \AA . The inset shows the normalized intensity line profile between the center of the diffraction pattern and the edge in the horizontal direction. The horizontal axis of the inset corresponds to the scale of the diffraction pattern along the horizontal direction.

The surface adsorption site density of the amorphous Mg_2SiO_4 film was estimated to be $\sim 10^{16}$ sites cm^{-2} according to the method described elsewhere (Hama et al. 2012; Tsuge et al. 2019), in which the known site density of an Al surface (1.2×10^{15} sites cm^{-2} , Wyckoff 1931) was used as a reference. This value is similar to that of the porous ASW surface, indicating the roughness of the film.

A.2. The effect of NSC during TPD process

Because in the TPD-REMPI measurements, we monitor the number density of $o\text{-H}_2$ upon sublimation, i.e., at $t = t_{\text{w.t.}} + t_{\text{TPD}}$ defined in Figure 1, the measured number density of $o\text{-H}_2$ is different from that at $t = t_{\text{w.t.}}$. From Equation (1), the number density of $o\text{-H}_2$ after a certain waiting time ($t = t_{\text{w.t.}}$) is derived as $[o\text{-H}_2]_{t=t_{\text{w.t.}}} = [o\text{-H}_2]_0 e^{-k_{\text{OP}} t_{\text{w.t.}}}$. During a TPD run, ortho-to-para conversion is accelerated. When we ignore the temperature (time) dependence of the conversion rate during TPD, the time evolution of $[o\text{-H}_2]$ is described as

$$[o\text{-H}_2]_{t=t_{\text{w.t.}}+t_{\text{TPD}}} = [o\text{-H}_2]_0 \times e^{-k_{\text{OP}} t_{\text{w.t.}} - k' t_{\text{TPD}}}, \quad (\text{A1})$$

where k' is the ortho-to-para conversion rate constant during TPD. By taking the logarithm of Equation (A1), we obtain

$$\ln([o\text{-H}_2]_{t=t_{\text{w.t.}}+t_{\text{TPD}}}/[o\text{-H}_2]_0) = -k_{\text{OP}} t_{\text{w.t.}} - k' t_{\text{TPD}}, \quad (\text{A2})$$

This relation suggests that a plot of $\ln([o\text{-H}_2]_{t=t_{\text{w.t.}}+t_{\text{TPD}}}/[o\text{-H}_2]_0)$ versus $t_{\text{w.t.}}$ gives a linear relation, and the rate constants k_{OP} and k' can be determined from the slope and intercept, respectively.

The experimental data obtained at 10 K (those shown in Figure 2b) are plotted in Figure A2. As expected, a plot of $\ln([o\text{-H}_2]_{t=t_{\text{w.t.}}+t_{\text{TPD}}}/[o\text{-H}_2]_0)$ versus $t_{\text{w.t.}}$ shows a

linear relation, and from the slope and intercept, we obtain $1/k_{OP} = 1050 \pm 90$ s and $1/k' = 220 \pm 50$ s. The $1/k_{OP}$ value (1050 ± 90 s) agrees well with the time constant (980 ± 90 s) determined from a single exponential fitting to $[o\text{-H}_2]_{t=t_{w.t.}+t_{TPD}}$, indicating that the latter value can be regarded as the time constant for ortho-to-para conversion during the waiting time. In addition, the ortho-to-para conversion time constant during the TPD run, $1/k' = 220 \pm 50$ s, which is slightly smaller than or equivalent to the constant determined for 18 K (260 ± 70 s), guarantees the validity of our analyses.

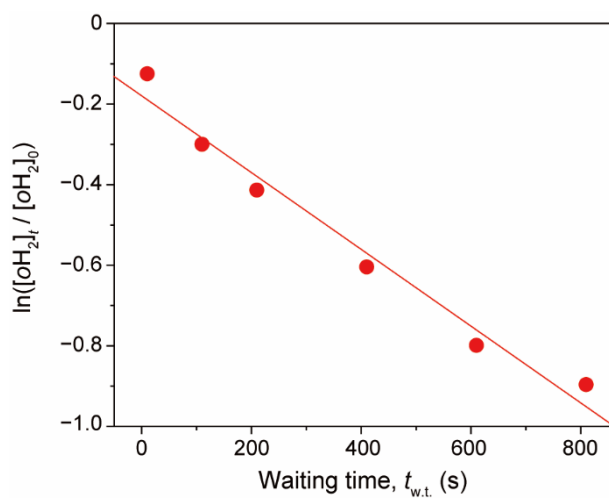


Figure A2. Additional analysis of the $J=1$ TPD-REMPI signal decay at 10 K. The values $\ln([o-H_2]_{t=t_{w.t.}+t_{TPD}}/[o-H_2]_0)$ are plotted versus $t_{w.t.}$ according to Equation (A2). The linear regression analysis result is shown by the solid line.

A.3. Para-to-ortho conversion of D₂ on a silicate surface

Because D₂ is a Boson due to two deuterons with nuclear spin 1, the nuclear spin state of 2 and 0 (ortho) and 1 (para) are only coupled with the rotational states of even and odd quantum numbers, respectively. Thus, at low temperatures, *ortho*- and *para*-D₂ are in the $J = 0$ and 1 states, respectively.

The para-to-ortho conversion of D₂ molecules on a silicate surface was investigated at 18 K. The time variation of integrated TPD-REMPI signals are plotted in Figure A3. The sum of $J = 0$ and $J = 1$ signals was constant within experimental error, ensuring that desorption of D₂ by thermal and upon NSC was negligible. Fitting of the $J = 1$ signal by a single exponential function gave a decay time constant of $2,200 \pm 300$ s. The NSC of D₂ is much slower than H₂, similarly to those on the ASW surface as previously reported ([Sugimoto & Fukutani 2011](#); [Ueta et al. 2016](#)).

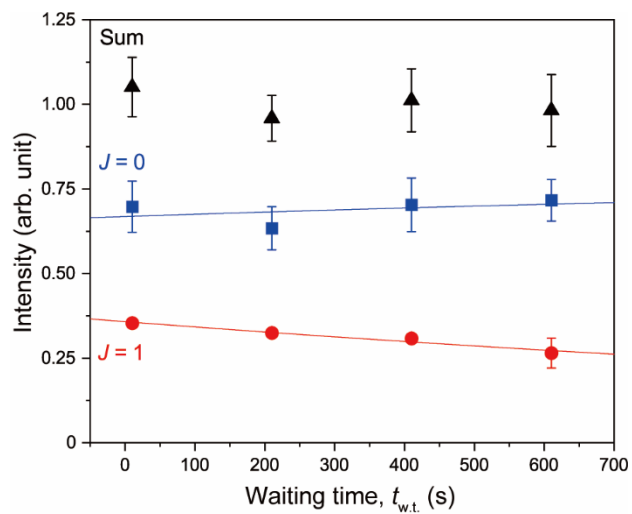


Figure A3. Time evolution of *ortho*-D₂ ($J = 0$) and *para*-D₂ ($J = 1$) populations at 18 K. The time evolution of TPD-REMPI signals for $J = 0$ (blue square), $J = 1$ (red circle), and their sum (black triangle). Intensities were obtained by integrating the TPD-REMPI signal. The error bars represent the statistical errors among 3 respective measurements. Solid curves are results of single exponential fitting.

References

- Bovino, S., Grassi, T., Schleicher, D. R. G., & Caselli, P. 2017, *ApJL*, 849, L25
- Chaabouni, H., Bergeron, H., Baouche, S., et al. 2012, *A&A*, 538, A128
- Flower, D. R., Pineau Des Forêts, G., Walmsley, C. M. 2006, *A&A*, 449, 621
- Fukutani, K., & Sugimoto, T. 2013, *PrSS*, 88, 279
- Furuya, K., Aikawa, Y., Hama, T., & Watanabe, N. 2019, *ApJ*, 882, 172
- Furuya, K., Aikawa, Y., Hincelin, U., Hassel, G. E., Bergin, E. A., Vasyunin, A. I., & Herbst, E. 2015, *A&A*, 584, A124
- Ghose, S., Hastings, J. M., Corliss, L. M., Rao, K. R., Chaplot, S. L., & Choudhury, N. 1987, *SSCom*, 63, 1045
- Hama, T., Kuwahata, K., Watanabe, N., Kouchi, A., Kimura, Y., Chigai, T., & Pirronello, V. 2012, *ApJ*, 757
- He, J., Acharyya, K., & Vidali, G. 2016, *ApJ*, 823, 56
- He, J., & Vidali, G. 2014, *FaDi*, 168, 517
- Hocuk, S., & Cazaux, S., 2015, *A&A*, 576, A49
- Honvault, P., Jorfi, M., González-Lezana, T., Faure, A., & Pagani, L. 2011, *PhRvL*, 107, 023201
- Hugo, E., Asvany, O., & Schlemmer, S. 2009, *JChPh*, 130, 164302
- Igami, Y., Tsuchiyama, A., Yamazaki, T., Matsumoto M., Kimura, Y. 2020, *GeCoA*, 293, 86
- Iisca, E. 2018, *CPL*, 713, 289
- Iisca, E., & Ghiglieno, F. 2014, *EPJB*, 87, 235
- Lee, T. J., Gowland, L., & Reddish, V. C. 1971, *NPhS*, 231, 193
- Pagani, L., Lesaffre, P., Jorfi, M., Honvault, P., González-Lezana, T., & Faure, A. 2013, *A&A*, 551, A38
- Planck Collaboration, Abergel, A., Ade, P. A. R., et al. 2014, *A&A*, 571, A11
- Scott, P. L., & Jeffries, C. D. 1962, *PhRv*, 127, 32
- Silvera, I. F. 1980, *RvMP*, 52, 393
- Sugimoto, T., & Fukutani, K. 2011, *NatPh*, 7, 307
- Tsuge, M., Hama, T., Kimura, Y., Kouchi, A., & Watanabe, N. 2019, *ApJ*, 878, 23
- Ueta, H., Watanabe, N., Hama, T., & Kouchi, A. 2016, *PhRvL*, 116, 253201
- Vaytet, N., Tomida, K., & Chabrier, G. 2014, *A&A*, 563, A85
- Wakelam, V., Bron, E., Cazaux, S., et al. 2017, *MolAs*, 9, 1
- Watanabe, N., Kimura, Y., Kouchi, A., Chigai, T., Hama, T., & Pirronello, V. 2010, *ApJL*, 714, L233
- Wilgenbus, D., Cabrit, S., Pineau des Forêts, G., & Flower, D. R. 2000, *A&A*, 356, 1010
- Wyckoff, R. W. G. 1931, *The Structure of Crystals* (New York: Chemical Catalog Co., Inc)